Aerodynamic characteristics of unsteady gap flow in a bristled wing

Seung Hun Lee, Mohsen Lahooti, and Daegyoum Kim

Articles you may be interested in

Numerical investigation of the breakup behavior of an oscillating two-phase jet
Physics of Fluids **30**, 072101 (2018); 10.1063/1.5029772

Vortex interaction with a rough wall formed by a hexagonal lattice of posts
Physics of Fluids **30**, 054107 (2018); 10.1063/1.5026463

Dynamics of a flexible superhydrophobic surface during a drop impact
Physics of Fluids **30**, 072102 (2018); 10.1063/1.5028127

Marangoni effect on the motion of a droplet covered with insoluble surfactant in a square microchannel
Physics of Fluids **30**, 077101 (2018); 10.1063/1.5026874

Analysis of disturbances in a hypersonic boundary layer on a cone with heating/cooling of the nose tip
Physics of Fluids **30**, 054103 (2018); 10.1063/1.5024025

Viscoelastic shear flow past an infinitely long and freely rotating cylinder
Physics of Fluids **30**, 073101 (2018); 10.1063/1.5037903

Aerodynamic characteristics of unsteady gap flow in a bristled wing

Seung Hun Lee, Mohsen Lahooti, and Daegyoum Kim[a)]
Department of Mechanical Engineering, KAIST, Daejeon 34141, South Korea

A micro-scale flying insect has a unique wing configuration consisting of a central frame and several bristles. For the low-Reynolds-number regime in which the insect lives, the bristled wing utilizes a virtual fluid barrier inside gaps produced by strong viscous diffusion of shear layers to overcome its morphological limitations. Considering the unsteady flapping motion of such a wing, the aerodynamic characteristics of gap flow formation are investigated numerically using a two-dimensional bristled wing model for a wide range of Reynolds numbers. Inside a gap between bristles, the development of a stopping vortex during the deceleration phase and its effect on the extinction of an existing vortex generated at the same edge are dependent on the Reynolds number, which leads to a significant change in vorticity distribution at stroke reversal even with just a small change in the Reynolds number. As the Reynolds number decreases, the gap flow responds more rapidly to wing motion, and its pattern does not deviate significantly from the kinematics of the wing. A noticeable difference is also observed in the behavior of the aerodynamic force acting on each bristle at low and high Reynolds numbers. With regard to aerodynamic force generation by the bristles, each bristle behaves independently and produces similar force because of strong gap flows relative to the wing at high Reynolds numbers. Meanwhile, at low Reynolds numbers, each bristle experiences a different force depending on its relative position, which indicates the existence of collective interaction of bristles through a virtual fluid barrier. *Published by AIP Publishing.* https://doi.org/10.1063/1.5030693

I. INTRODUCTION

Flying insects are able to achieve surprisingly high propulsive performance by generating unsteady flow structures, and it has been suggested that a similar approach be adopted to significantly improve the aerodynamic capabilities of micro air vehicles. However, understanding the principles of unsteady propulsion mechanisms remains a challenging task, although the mechanisms of lift augmentation during unsteady motion have been extensively studied by many research groups.[1–3] Although numerous studies to uncover the aerodynamics of unsteady wings have been conducted, most of these have been based on typical wing shapes with a continuous surface. The wings of a fairyfly (the smallest known flying insects) and a thrips, in contrast to those of most insects, have a very distinct configuration: the so-called comb-like or bristled wings.[4,5] As can be seen in the figures in the work of Huber and Noyes,[5] a bristled wing consists of a single main frame at the center, from which several bristles extend in all directions, with gaps between them.

In nature, this morphological characteristic of a propulsor with gaps is not limited to small flying insects such as a fairyfly and a thrips. Some other small organisms control leakage through gaps by changing the size and speed of the gaps, i.e., by changing the Reynolds number. If the Reynolds number is small enough, strong viscous diffusion causes a thick shear layer to develop along the surface of the gap and eventually overlap the latter. Leakage through the gap is thereby drastically reduced. This phenomenon has been revealed by previous studies on propulsive lappets of a juvenile jellyfish[6,7] and on hairy organs for food detection[8] and olfactory sensing.[9,10]

A fairyfly and a thrips, which live in the low-Reynolds-number regime [$Re = O(10)$], also utilize a virtual fluid barrier formed in the gaps of their wings as a result of overlapping thick shear layers, so they are able to fly with the peculiar geometry of a bristled wing. Sunada *et al.*[11] conducted a pioneering study on a translating or rotating bristled wing model, in which a bristled wing in the low-Reynolds-number regime [$Re = O(10)$] was found to generate a comparable, but slightly smaller, aerodynamic force to that generated by a smooth wing. They obtained high lift and drag coefficients of the bristled wing because the reduction in wing area is greater than the reduction in lift and drag forces. A theoretical analysis of a creeping flow around a row of slender bodies showed that more than 95% of the flow detours around the row, instead of passing through the gaps.[12] Weihs and Barta[13] studied fluid leakage and aerodynamic force generation in each bristle along the spanwise direction of a flapping bristled wing, for which the flapping velocity increases linearly from the root of the wing to its tip in the Stokes flow regime. Davidi and Weihs[14] presented the velocity distribution between gaps for several Reynolds numbers and obtained the limits on the Reynolds number at which the performance of a bristled wing is comparable to that of a smooth wing. Recently, Lee and Kim[15] investigated flow structures in both initial transient and quasi-steady phases of a translating three-dimensional comb wing for wide ranges of gap size, angle of attack, and the Reynolds number.

Past studies on bristled wings have considered mainly simple kinematics such as translation with constant velocity.

---

a)daegyoum@kaist.ac.kr

Although these studies on steady wing motions have been important in revealing the fundamental aerodynamic mechanisms of bristled wings, the actual unsteady characteristics of insect wing motions need to be taken into consideration for a better understanding of the complicated flight of insects.[16] Santhanakrishnan *et al.*[17] and Jones *et al.*[18] studied an unsteady lift generation mechanism of bristled wings, namely, clap and fling, by considering the actual kinematics of such wings and claimed that airflow through the wing surfaces reduces the drag required to fling them apart and thus increases the average lift-to-drag ratio during a flapping cycle.

In spite of emerging interest in the aerodynamics of bristled wings, however, previous studies on unsteady wing motions have been confined to finding correlations between propulsive performance and wing configuration, rather than describing the development of gap flow, which is critical for determining the overall flow structure and its effect on aerodynamic performance. The formation of gap flow is expected to be more important in a flapping bristled wing because the wing continues to reciprocate within a short distance and an unsteady flow structure repeats to generate per each stroke. Nevertheless, little information is available on the formation of gap flow in a bristled wing under periodic flapping motion, although gap flow formation after the onset of motion has been investigated for a translating bristled wing.[15] In the present study, the unsteady formation of gap flow in a bristled wing and its aerodynamic characteristics are numerically investigated for a wide range of Reynolds numbers between 1 and 100. We consider both an oscillating bristled wing with a constant angle of attack and a flapping bristled wing combined with a pitching motion. First, for the simple oscillating bristled wing, we examine the development of gap flow, the behavior of fluid particles around the wing, the force acting on each bristle, and finally the effect of the Reynolds number on the formation of gap flow. Then, we expand our analysis to the case of a flapping wing by adding pitching motion to the oscillating motion.

II. PROBLEM DESCRIPTION

A. Wing model

In a bristled wing, bristles near the mid-span of the wing extend in the chordwise direction, whereas bristles near the wing tip extend in the spanwise direction;[4,5] also see Figs. 1(a) and 1(b) for *Frankliniella occidentalis*, a species of thrips. As in the study of Jones *et al.*,[18] here we introduce a simplified two-dimensional bristled wing which captures the characteristic of the actual bristled wing. Our model consists of five equally spaced bristles, and the width of the gaps between bristles is equal to the width of a bristle Figs. 1(c) and 1(d). This width is taken as $\frac{1}{9}c$, where c is the total chord length of the wing ($c = 1$ in our computational model). The thickness of the wing is $\frac{1}{1000}$ of the chord length, which is sufficiently small that the effect of thickness can be neglected.

Two representative motions are considered separately: translational oscillation without rotation [*oscillating*: Fig. 1(c)] and a combination of translational oscillation and periodic pitching motion [*flapping*: Fig. 1(d)]. For the oscillating
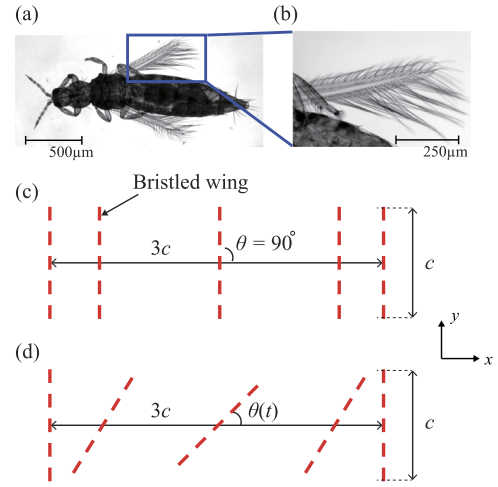

FIG. 1. [(a) and (b)] Micrographs of (a) *Frankliniella occidentalis*, a species of thrips, and (b) its wing. [(c) and (d)] A simplified two-dimensional bristled wing model (red) inspired by the biological bristled wing. The wing model has five bristles equally spaced. The motions of the wings are illustrated at several instances for (c) oscillating motion and (d) flapping motion. In (d), only a half-cycle is depicted for the motion from left to right. The actual thickness of the wing model is much smaller than it appears in this figure.

motion, the kinematics are as follows:

$$x(t) = x_0 \sin(2\pi f t), \tag{1}$$

where x_0 and f are the amplitude and frequency of oscillation, respectively, where $x_0 = 1.5$ and $f = \frac{1}{3}$. The angle of attack θ with respect to the horizontal axis is fixed as 90° [Fig. 1(c)]. For the flapping motion, the rotational motion of the wing is added and is prescribed as

$$\theta(t) = 90° - \theta_0 \sin(2\pi f t + \pi/2), \tag{2}$$

where $\theta_0 = 45°$ is the amplitude of rotation [Fig. 1(d)]. The pitching axis is located at the middle of the chord.

The aim of this study is to investigate the dynamics of shear layers inside the gaps and their effects on force generation of each bristle, rather than exploring the effects of variations in geometric and kinematic parameters or the biomechanics of an insect wing. For this reason, we consider only a single model as shown in Fig. 1 for the geometry and Eqs. (1) and (2) for the kinematics. In the present study, the data of one cycle will be analyzed after an initial transient phase of about four to five cycles.

The Reynolds number based on the chord length and flapping speed of a biological bristled wing is known to be about 10; the bristle-diameter-based Reynolds number is near $O(10^{-2})$.[17,18] To examine the effect of viscosity, the range of Reynolds numbers $Re = \overline{U}c/\nu$ in this study is between 1 and 100 ($Re = 1, 3, 10, 30,$ and 100), including the Reynolds number relevant to actual bristled wings ($Re \approx 10$). $\overline{U} = 4x_0 f$ is the mean flapping speed, ν is the kinematic viscosity of the fluid, and c is the chord length. The flow around the wing is assumed to remain two-dimensional in the Reynolds number range of this study.[19] As characteristic length scale in the definition of the Reynolds number, the gap size between bristles or the width of a bristle can be used as well. However, the chord length c was chosen for the Reynolds number definition because it has been used conventionally in aerodynamics

community, including our previous study.[15] The Reynolds number based on the gap width can be computed easily by dividing the Reynolds number given in this study by 9: gap width = chord/9. x- and y-directional force coefficients are defined as

$$C_x(t) = \frac{2F_x(t)}{\rho \overline{U}^2 c} \quad \text{and} \quad C_y(t) = \frac{2F_y(t)}{\rho \overline{U}^2 c}. \quad (3)$$

B. Numerical method

For numerical simulation of a thin object moving in two-dimensional incompressible laminar flow, an in-house code was developed, which is based on the sharp-interface hybrid Cartesian/immersed boundary (HCIB) method.[20] Here, we simply summarize our approach. For the complete solution procedure of the HCIB method including a ray-tracing algorithm for the identification of an immersed body, see the studies of Gilmanov and Sotiropoulos,[20] Ge and Sotiropoulos,[21] and Borazjani, Ge, and Sotiropoulos.[22] The discretization of the governing equations is based on a finite difference method in Cartesian coordinates with a three-time-level second-order difference scheme for time, a second-order linear upwind scheme for convective terms, and a standard central difference scheme for diffusive terms. Both linear diffusive terms and nonlinear convective terms are treated implicitly. However, owing to the nonlinear treatment of convective terms, the system of equations is nonlinear and is solved using Newton's method in combination with the matrix-free generalized minimal residual method (GMRES).[23,24] The fractional step method of Van Kan[25] is employed for pressure–velocity coupling on a collocated grid layout. A collocated grid arrangement is preferred to a staggered grid arrangement in order to avoid the complications that would arise with the latter due to the enforcement of boundary conditions on an immersed object. However, the collocated layout can lead to a so-called checker-board situation. To avoid this problem, as proposed by Gilmanov and Sotiropoulos,[20] the momentum equations are discretized on collocated grids, and the discretized equations are interpolated to cell faces via a third-order one-dimensional QUICK interpolation, while velocities are updated on cell faces instead of cell centers.

In our simulations, a rectangular fluid domain of total domain size $[-49c, 49c] \times [-21c, 21c]$ is constructed. The origin of this fluid domain is identical to the location of the pitching axis in mid-stroke. The fluid domain consists of two regions: uniform square grids near the wing ($[-2c, 2c] \times [-1c, 1c]$) with a spacing $dx = dy = 0.0075c$ and nonuniform rectangular grids with exponentially increasing size outside the uniform grid region. The total number of grids is $N_x \times N_y = 775 \times 507$. The time step is determined by a criterion based on the Courant–Friedrichs–Lewy (CFL) number, which restricts a Lagrangian point on the wing to passing through less than one grid of the fluid domain in each time step. In our simulation, 4000 time steps are used for a single cycle.

To check grid convergence, we varied the grid spacing around the wing from $dx = dy = 0.0075c$ to $dx = dy = 0.01c$ for the same domain size at $Re = 10$ and compared the average x- and y-directional force coefficients of a flapping bristled wing for one cycle. Here, the average x- and y-directional
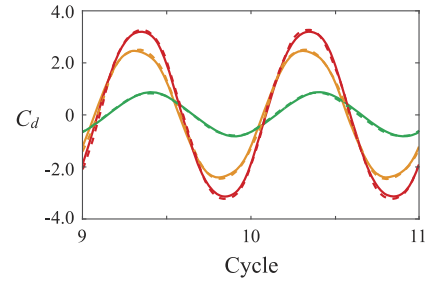

FIG. 2. Time histories of total drag (red), drag by pressure (orange), and drag by viscous stress (green) for an oscillating circular cylinder during two cycles: solid line (present work) and dashed line (Ref. [1]). $Re = 100$ and $KC = 5$.

force coefficients are defined as $\overline{C}_x = \int_0^T |C_x(t)| \, dt/T$ and $\overline{C}_y = \int_0^T C_y(t) \, dt/T$, respectively. $\overline{C}_y$ and $\overline{C}_x$ of a flapping bristled wing during one cycle were, respectively, 3.77 and 1.11 for the coarse-grid case ($0.01c$) and 3.97 and 1.09 for the fine-grid case ($0.0075c$). The difference between the two cases is just within 5%, which is small enough to confirm that our results are reliable.

C. Code validation

To validate our in-house immersed boundary method (IBM) code, we conducted two sets of tests. Note that the definition of some parameters in this section may differ from the definition of some parameters in Secs. II A and II B. First, for the problem including a moving object, we compared our results for a harmonically oscillating circular cylinder with diameter d to those of Dütsch et al.[26] Non-uniform grids with minimum spacing $0.01d$ near the cylinder are constructed for a rectangular fluid domain of $[-20d, 20d] \times [-15d, 15d]$. The total number of grids is $N_x \times N_y = 584 \times 472$. In this validation test, translational motion $x(t)$ is given as $x(t) = A \sin(2\pi ft)$, where A and f, respectively, denote the amplitude and frequency of the cylinder motion. The Reynolds number $Re = U_{max} d/\nu$ and the Keulegan-Carpenter number $KC = U_{max}/fd$ are 100 and 5, respectively, where U_{max} is the maximum speed of the cylinder. The drag coefficient C_d defined as $C_d(t) = 2F_x(t)/\rho U_{max}^2 d$ is compared with that of Dütsch et al.[26] in Fig. 2; in addition to the total drag, the drag by pressure and the drag by viscous stress are also compared.

Next, to validate our code in the Reynolds number much lower than 100, a stationary circular cylinder with diameter d in uniform free stream is considered. Non-uniform grids with minimum spacing $0.01d$ near the cylinder are constructed for a fluid domain of $100d$ in both x and y directions. The cylinder is located in the middle of the domain. The total number of grids is $N_x \times N_y = 394 \times 394$. The drag coefficient of a cylinder ($C_d = 2F_x/\rho U^2 d$) at $Re(=Ud/\nu) = 1$ is compared with other references in Table I. Figure 2 and Table I ensure that the results

TABLE I. Comparison of the drag coefficient for a circular cylinder in uniform free stream at $Re = 1$.

	Present work	Tritton[27]	Hamielec and Raal[28]	Sheard et al.[29]
$Re = 1$	11.3	10.9	11.0	11.7

of our in-house code are reliable in the Reynolds number range considered in our work.

III. RESULTS AND DISCUSSION

A. Oscillating bristled wing

We first investigate an oscillating bristled wing [Fig. 1(c)]. It is well known that, at a low Reynolds number [$Re = O(10)$], a gap in a bristled wing is blocked aerodynamically by viscous diffusion of two shear layers generated by the two edges of the gap, which is why a bristled wing has superior performance to a wing with a solid surface in terms of lift per unit actual wing surface area.[11–15] However, the velocity of the fluid in the gap does not coincide exactly with that of the wing surface in the low-Reynolds-number regime. For example, for a bristled wing at a low Reynolds number [$Re = O(10)$], the flow velocity in a gap clogged by shear layers reaches about 80% of the wing velocity in the quasi-steady phase of translational motion.[14,15] For a translating bristled wing, as the gap size becomes smaller, the gap flow responds more rapidly to the wing kinematics; i.e., the flow velocity in the gap becomes close to the wing velocity in a shorter time because it requires less time for the shear layers to form a virtual fluid barrier.[15] Obviously, the flow velocity in the gaps of a bristled wing undergoing horizontally reciprocating motion [Fig. 1(c)], or under any unsteady kinematics, does not remain constant because of the repeated formation and extinction of the shear layers in each stroke. Lee and Kim[15] addressed the initial development of gap flow for the starting phase of a steady translation. However, in an oscillating bristled wing, it is important to understand how the acceleration and deceleration of the oscillating wing affect the development of gap flow and shear layers.

Since, at $Re = 10$, the flow field of an oscillating wing is symmetric with respect to the middle of the chord,[30] we present only the upper half of the wing in Fig. 3(a) (Multimedia view). In our study, no noticeable asymmetry between the upper and lower halves of the wing is found at $Re = 10$. Meanwhile, at a relatively large Reynolds number (e.g., at $Re = 100$ in our study), we observe symmetry breaking of the flow structure, although, for simplicity, we present only the upper half of the wing for $Re = 100$ in Fig. 3(a) (Multimedia view). The schematics of vortex formation near the first and second bristles from the top of the wing are shown in Fig. 3(b), where the red and blue circles indicate the direction and magnitude of the vortex, respectively.

The dimensionless vortex circulation, defined as $\Gamma^* = \int \omega \, dA/\overline{U}c$, is obtained for the vortices generated by the outermost edge of the wing (outer-edge vortex) and the inner edge of the gap (gap vortex). To include desired vorticity for the circulation, time-varying integration area A is set as $[-2c, x(t) + 0.5c] \times [0.44c, 1c]$ for the outer-edge vortex and $[-2c, x(t) + 0.5c] \times [0.33c, 0.44c]$ for the gap vortex [Fig. 4(c)]. $x(t)$ is the instantaneous position of the wing, and $y = 0.44c$ corresponds to the overlapped line of solid and dashed areas in Fig. 4(c), where the center of the first bristle is located. For the right end of the integration area, $0.5c$ in front of the wing is additionally considered to include vorticity diffused in front of the wing which is noticeable at low Re. With the
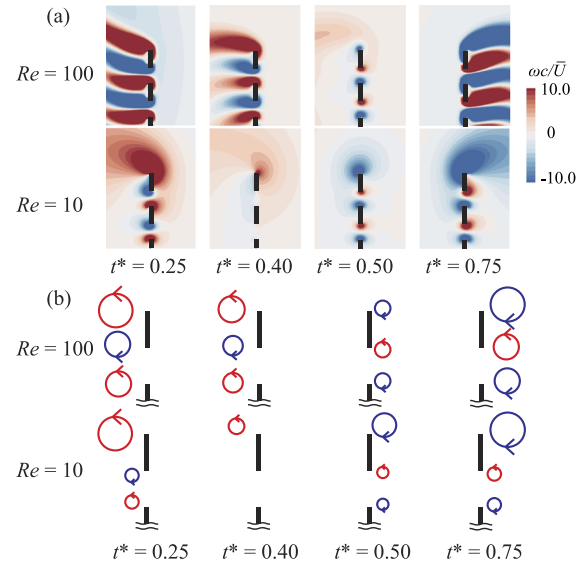

FIG. 3. (a) Vortex structure around an oscillating bristled wing at $Re = 100$ and 10. In (a), only the upper half of the wing is presented. (b) Schematics of the vortex structure corresponding to (a). The arrows indicate the rotating direction of the vortex. The black lines represent the bristles of the wing. Note that the thickness of the bristles is magnified from their actual thickness. Multimedia view: https://doi.org/10.1063/1.5030693.1

integration area chosen carefully by examining vorticity contours, we were able to exclude vorticity generated by the previous stroke or the other segments of the wing. To avoid including noise, the threshold values of the dimensionless vorticity $\omega c/\overline{U}$ were chosen as 0.5 for the outer-edge vortex and -0.5 for the gap vortex. The time histories of circulation computed with several vorticity thresholds, $|\omega c/\overline{U}| = 0 - 3.0$, are presented in the Appendix (Fig. 13). In Fig. 13, the deviation in the circulation of the outer-edge vortex is pronounced as the threshold becomes larger than 1.0, while the circulation of the
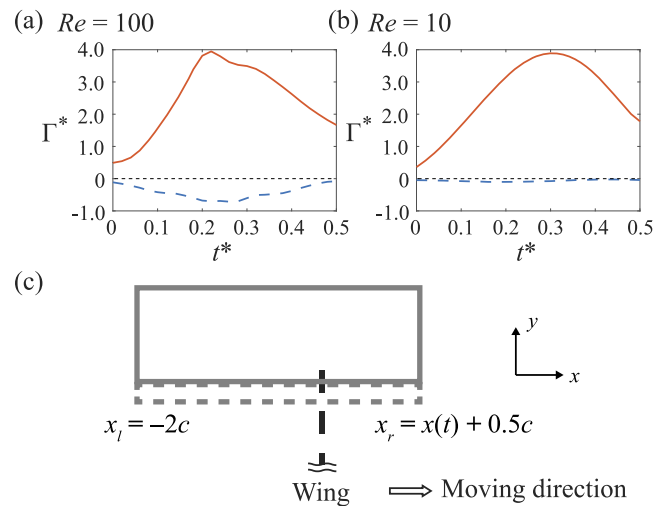

FIG. 4. [(a) and (b)] Time history of nondimensional circulation $\Gamma^*(= \Gamma/\overline{U}c)$ for (a) $Re = 100$ and (b) $Re = 10$. The solid and dashed curves represent the circulations obtained inside solid and dashed areas, respectively, depicted in (c). The red and blue colors indicate positive and negative circulations, respectively. (c) Integration areas for circulation. The right ends of the areas extend ($x_r = x(t) + 0.5c$) as the wing translates to the right, while the left ends are fixed ($x_l = -2c$).

gap vortex remains nearly unaffected by the threshold value. Hence, we chose the threshold of $|\omega c/\overline{U}| = 0.5$ which shows the trend similar to the case of $|\omega c/\overline{U}| = 0$.

In Fig. 3 (Multimedia view), for $Re = 100$, a strong negative-vorticity region is observed inside the gap at $t^*(=t/T) = 0.25$, which corresponds to the mid-stroke of maximum velocity, and the gap vortex is elongated to the leeward of the wing. See also Fig. 4(a) for the strength of the negative-vorticity region: $|\Gamma^*| = 0.70$ at $t^* = 0.25$. At this moment, the circulation of the positive-vorticity region of the solid area near the outermost edge $|\Gamma^*|$ is 3.71. Meanwhile, for $Re = 10$, the negative vorticity of the dashed area is confined near the gap instead of extending to the leeward of the wing, because, at a low Reynolds number, two counter-rotating gap vortices that have developed at the two edges of the gap cancel each other quickly owing to rapid diffusion of vorticity.[6,15] As a result, the strength of the negative gap vorticity ($|\Gamma^*| = 0.09$) is less than 3% of the strength of the positive outer-edge vorticity ($\Gamma^* = 3.67$) at $t^* = 0.25$ [Fig. 4(b)].

As a wing decelerates suddenly or stops, the fluid that moves behind the wing starts to turn forward around the wing and evolve a vortex of opposite sign, which is called a stopping vortex. In general, the generation of the stopping vortex and its interaction with the existing vortex is important in determining the overall propulsive performance of a flapping propulsor.[31] A stopping vortex is also found at the gap and at the outer edge of a decelerating bristled wing. As the wing decelerates after $t^* = 0.25$, vorticity is generated at the edges, with opposite sign to the vorticity formed during the accelerating phase ($0 < t^* < 0.25$), and eventually annihilates the latter Figs. 3(a) and 3(b) (Multimedia view). In the acceleration phase following the stroke reversal ($t^* = 0.50$–0.75), the new vortex structure that started to form during the deceleration phase becomes more prominent.

At the lower Reynolds number ($Re = 10$), because of stronger viscous diffusion, gap vorticity is small at mid-stroke, which is followed by rapid diffusion of the stopping vortex during deceleration. Thus, the extinction of the original gap vortex formed during the accelerating phase occurs shortly after the beginning of deceleration at a lower Reynolds number. That is to say, the Reynolds number determines the extinction of the existing gap vortex and the generation of the new gap vortex of opposite sign. For instance, at $t^* \approx 0.40$, for $Re = 100$, the strong gap vortex of negative vorticity that has grown during the acceleration phase is still observed; its circulation $|\Gamma^*|$ is 0.38. Meanwhile, for $Re = 10$, the gap vortex almost disappears, $|\Gamma^*| = 0.03$ (Fig. 4). For $Re = 100$, the moment when the sign of the gap vortex or the outer-edge vortex changes is between $t^* = 0.45$ and 0.50, which is delayed compared to the $Re = 10$ case ($t^* = 0.40$–0.45). Regardless of the Reynolds number, the process of stopping-vortex formation and resultant annihilation of the existing vortex occurs before the wing reaches the end of its stroke ($t^* = 0.50$).

For $Re = 100$, stopping vortices emerge both at the gap and at the outermost edge near $t^* = 0.45$, and their cores are clearly observed at $t^* = 0.50$, where both have the vorticity distribution of similar magnitude Figs. 3(a) and 3(b) (Multimedia view). Meanwhile, for $Re = 10$, the outer-edge vortex that has grown during acceleration still remains noticeable at $t^* = 0.40$

with its circulation $|\Gamma^*|$ of 3.24, while the gap vortex almost disappears. The rapid diffusion of vorticity inside the gap leads to its annihilation with the counter-rotating vortex generated by the other edge of the gap. However, the outer-edge vortex is not bounded by an edge and annihilation of vorticity does not happen, which helps us to maintain large circulation Figs. 3(a) and 3(b) (Multimedia view). For the same reason, during $t^* = 0.45$–0.75, the negative circulation of the outer-edge vortex which is not bounded by another edge increases earlier and more rapidly than the positive circulation of the gap vortex.

In addition to vortex strength, the temporal velocity profile inside the gap is also dependent on the Reynolds number (Fig. 5). Note that in Fig. 5, the red and blue arrows for a representative gap flow are drawn in a reference frame fixed to the wing. For a high Reynolds number ($Re = 100$), since there is little blocking effect by the shear layer, the minimum $u_{rel}/\overline{U}$ is -2.4 at mid-stroke [Fig. 5(b)]. The large inertia of the high-speed gap flow moving to the left during the acceleration phase slows the response of the gap flow to the wing kinematics during the deceleration phase. Thus, a negative x-directional flow with minimum $u_{rel}/\overline{U} = -1.1$ is still observed at $t^* = 0.40$. On the other hand, when the Reynolds number is low ($Re = 10$), because of the short time scale of diffusive momentum transfer and the small inertia of the relative gap flow, the gap flow becomes more agile in its response to the wing kinematics. The minimum $u_{rel}/\overline{U}$ at $Re = 10$ is -0.7 at mid-stroke, the magnitude of which is much smaller than that at $Re = 100$ [Fig. 5(c)]. Furthermore, there is nearly zero net flow through the gap at $t^* = 0.40$: $u_{rel}/\overline{U} \approx 0$. The greatest difference in the gap flow pattern between the two Reynolds number regimes is observed at $t^* \approx 0.40$, when the flow is in different directions
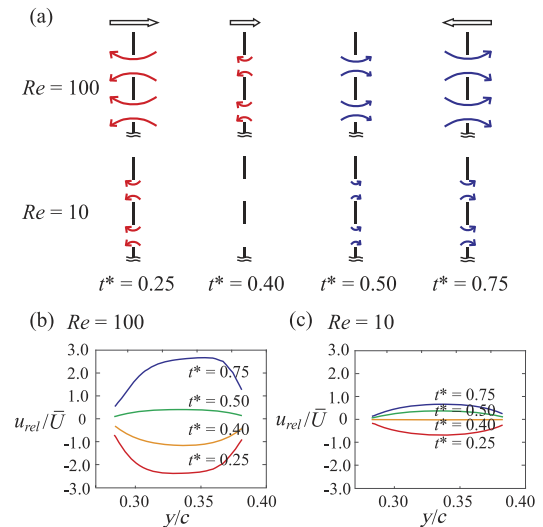

FIG. 5. (a) Schematics of the flow direction *with respect to the wing* during the deceleration and acceleration phases. The hollow arrows represent the absolute velocity of the wing. The red and blue arrows indicate the direction and magnitude of the gap flow, which are presented with respect to a reference frame fixed to the wing. The lengths of the arrows in the figure represent their approximate magnitude. Only the upper half of the wing is presented. The x-velocity distribution relative to the wing (u_{rel}) within the uppermost gap of the wing for (b) $Re = 100$ and (c) $Re = 10$. u_{rel} is normalized by the mean oscillating speed $\overline{U}$. In (b) and (c), $t^* = 0.25$ (red), 0.40 (orange), 0.50 (green), and 0.75 (blue).

in the two regimes. In the low-Reynolds-number regime, the reversed gap flow [blue arrows in Fig. 5(a)] after $t^* \approx 0.40$ also remains relatively small, owing to the rapid diffusion of the shear layer.

We have examined the pattern of gap flow with a special focus on its direction and magnitude during the deceleration phase and have revealed its dependence on the Reynolds number. However, an Eulerian description with vorticity and velocity distributions at several times may not be enough to fully understand the development of the gap flow under unsteady wing kinematics. Here, we consider the trajectory of fluid particles in order to demonstrate how drastically the gap flow pattern changes near stroke reversal as the Reynolds number varies between 10 and 100 (Fig. 6). In Fig. 6, fluid tracers (fluid particles) are arranged in the left (blue) and right (red) sides of the wing at $t^* = 0.25$. At $Re = 100$, red particles deeply penetrate the wing through the gaps. The maximum penetration depth is about $0.8c$ at $t^* = 0.40$, which is almost two-thirds of the displacement of the wing from $t^* = 0.25$ to $t^* = 0.40$. As the direction of the gap flow relative to the wing is reversed at $0.40 < t^* < 0.50$ (Fig. 5), penetrated red particles are pulled back toward the wing. While the wing moves from end-stroke ($t^* = 0.50$) to mid-stroke ($t^* = 0.75$) after stroke reversal, a significant number of red particles pass through the gaps to the right side of the wing because of the large inertia that they acquired in the previous stoke.

However, at a low Reynolds number ($Re = 10$), interestingly, most of the blue fluid particles behind the wing follow the wing from $t^* = 0.25$ to 0.40. Most of the red fluid particles in front of the wing turn around the wing, whereas only a small portion penetrate through the gaps. At $t^* = 0.40$, although the wing translates about $1.2c$ from mid-stroke, the red particles penetrate only about $0.2c$, whereas they penetrate $0.8c$ at $Re = 100$ for the same time span. From $t^* = 0.40$ to 0.50, the red particles tend to move through the gaps in the reverse direction, from left to right with respect to the wing. Therefore, at the end of the stroke ($t^* = 0.50$), just as at mid-stroke, most of the blue and red particles are positioned on the left and right sides of the wing, respectively. As the wing moves to the left after stroke reversal, blue particles leak through the gaps to the right side of the wing because of their inertia. At stroke reversal, the shear layer is not sufficiently developed to prevent penetration of the blue particles to the right

side. Although not studied here, in the case of creeping flow ($Re < 1$), we expect the penetration of fluid particles to be hardly observable and the bristled wing to exhibit a clearer paddle-like behavior.[8,12,32]

As mentioned above, only two Reynolds numbers ($Re = 10$ and 100) have been considered in order to present a clear description of how viscous diffusion of vorticity and momentum affects the pattern of gap flow during the deceleration phase and stroke reversal. We have revealed that the gap flow pattern varies drastically when the Reynolds number changes by just one order of magnitude from $O(10^2)$ to $O(10)$. In the range from $Re = 1$ to 100, the effect of the Reynolds number on the velocity of the gap flow is shown in Fig. 7(a). An average x-directional velocity $\hat{u}$ within the gaps was obtained by averaging *absolute* velocities of all nodes on a vertical line inside the four gaps. For $Re \le 10$, the time history of $\hat{u}$ inside the gaps does not deviate significantly from the velocity profile of the wing and preserves a sinusoidal shape [Fig. 7(a)]. The positive peak of $\hat{u}$ occurs at $t^* = 0.26$ for $Re = 1$ and at $t^* = 0.30$ for $Re = 10$ [Fig. 7(c)]. However, as the Reynolds number increases above 10, the phase of $\hat{u}$ is delayed drastically with respect to the wing velocity; the time of the positive peak of $\hat{u}$ increases monotonically with increasing Reynolds number [Fig. 7(c)]. For a high Reynolds number, since the formation of a virtual barrier inside the gap is delayed or does not occur, the gap flow cannot keep up with the kinematics of the wing. See the difference between $Re = 10$ and $Re = 100$ at $t^* = 0.40$ in Figs. 5(a) and 5(c). For $Re = 100$, the positive peak of $\hat{u}$ is even at $t^* = 0.68$, after stroke reversal. As Re increases from 1, in addition to the phase shift, the peak magnitude of the x-velocity gradually becomes smaller because of increased fluid leakage through the gap [Fig. 7(a)]. For example, the maximum of $\hat{u}/\overline{U}$ falls from 1.44 at $Re = 1$ to 0.84 at $Re = 30$ and to 0.54 at $Re = 100$. Although Barta[32] reported the lag of flow in oscillating slender bodies in creeping flow, it becomes more pronounced as the order of the Reynolds number is greater than 1 Figs. 7(a) and 7(c).
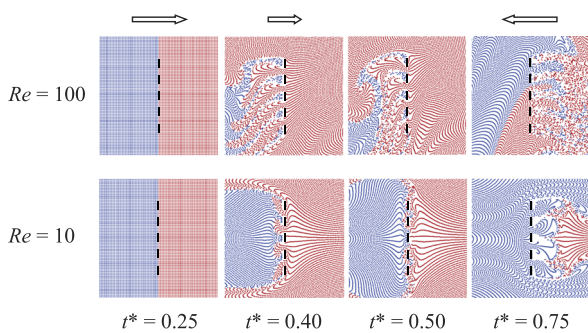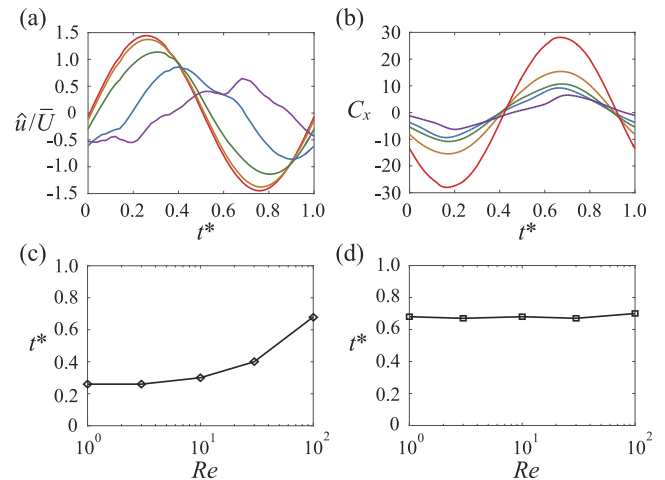

FIG. 6. Movement of fluid particles initially aligned around the wing at $t^* = 0.25$. The hollow arrows represent the absolute velocity of the wing, as in Fig. 5. In this figure, the thickness of the bristles is magnified from their actual thickness.

FIG. 7. (a) x-directional velocity $\hat{u}$ averaged for the entire four gaps in the wing during one cycle, and normalized by the mean speed of oscillation $\overline{U}$. (b) X-directional force acting on the entire wing during one cycle. In (a) and (b), $Re = 1$ (red), 3 (orange), 10 (green), 30 (blue), and 100 (purple). Phases of the positive peaks for x-directional velocity (c) and x-directional force coefficient (d) as functions of the Reynolds number.

On the other hand, in contrast to the gap flow velocity $\hat{u}$, the time history of the x-directional force coefficient C_x remains sinusoidal for all Reynolds numbers Figs. 7(b) and 7(d). Although the magnitude of the positive peak of C_x decreases with increasing Reynolds number, the phase of its positive peak is almost constant ($t^* = 0.67$–0.70), despite the change in the Reynolds number. That is, the phase of virtual barrier formation does not directly affect the phase of force generation, but rather the magnitude of force.

B. Aerodynamic force on individual bristles

For a bristled wing, if viscous diffusion is strong enough to allow the interaction between close bristles, the aerodynamic force exerted on each bristle depends on its relative position. Figure 8 shows how the forces in the x- and y-directions acting on each bristle change with the Reynolds number for the oscillating motion. To obtain the force coefficients C_x and C_y for a single bristle, the total chord length c is used in their definitions in Eq. (3), instead of the width of a bristle. For $Re = 100$, with regard to the magnitude and phase of C_x, no regular order of bristles is observed during a cycle, and each bristle seems to behave independently [Fig. 8(a)]. The viscous shear layer inside the gap is so thin that it does not affect a neighboring bristle. The bristled configuration can be regarded as the collection of independent small segments arranged side-by-side.

Meanwhile, for $Re = 10$, the absolute magnitude of C_x acting on the two outer bristles (red and black in Fig. 8) is slightly greater than that for the two inner bristles (orange and blue); the absolute maximum value of C_x is 2.22 at the outer bristles and 2.08 at the inner bristles [Fig. 8(c)]. Each inner bristle moves in the flow field induced by adjacent bristles, while each of the outer bristles is confined by only one nearby bristle, which results in the discrepancy in C_x.[8,12,14] Furthermore, differences are observed in the phase of the force peak, as well as in its magnitude. The positive peak of C_x for the inner bristles is slightly ahead, by about $T/100$, of the two outer bristles. During the deceleration phase, the extinction
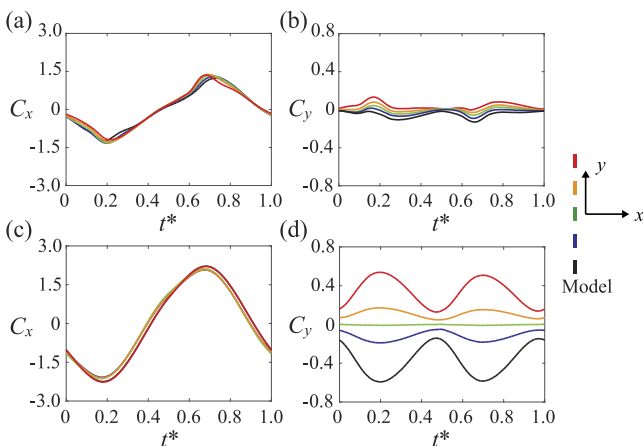
of the outer-edge vortices of the wing is slightly slower than that of the gap vortices, as depicted in Fig. 3 (Multimedia view), which may lead to the minor difference in the peak phase.

A noticeable difference between $Re = 100$ and $Re = 10$ is found in C_y rather than in C_x Figs. 8(b) and 8(d). Because of the thin geometry, the y-directional force C_y is mostly caused by the viscous force acting on the bristle rather than the pressure force. For $Re = 100$, no significant y-directional force appears at each bristle: $|C_y| < 0.13$ during one cycle for all bristles [Fig. 8(b)]. At this high Reynolds number, the flow around each bristle is nearly symmetric with respect to the center of the bristle because of a strong gap flow and the independent formation of vortices at the edges of the bristle, which results in a negligible C_y for each bristle.

However, for $Re = 10$, bristles at the same distance from the center of the wing produce C_y of the same magnitude but different sign [Fig. 8(d)]; i.e., the distribution of C_y is symmetric with respect to the entire wing. In contrast to the behavior of C_y at $Re = 100$ [Fig. 8(b)], the maximum value of C_y at $Re = 10$ exists near mid-stroke and the minimum value near end-stroke. At end-stroke, in spite of the zero wing velocity, C_y is nonzero for all but the center bristle (green). More interestingly, the difference in C_y among the five bristles is obvious when compared with the case of $Re = 100$, and the order of C_y magnitude among the five bristles is consistent through a cycle. The maximum and minimum magnitudes of C_y for the outer bristles (red and black) are 0.59 and 0.13, respectively, while the maximum and minimum magnitudes of C_y for the inner bristles (yellow and blue) are 0.19 and 0.05, respectively; the center bristle has almost zero C_y during a cycle.

Although the magnitude of C_y is smaller than that of C_x throughout a cycle, it is noteworthy that a huge deviation among the bristles is found in C_y rather than C_x. At a low Reynolds number, owing to the virtual barrier caused by a gap, the flow tends to turn around the outer edges of the wing instead of penetrating through the gaps (Fig. 6). That is to say, while each bristle seems to function separately in the high-Re regime, an array of bristles acts like a single continuous body in the low-Re regime. The detour of the flow around the outer edges of the wing induces a viscous force in the y-direction greater than that at a high Reynolds number ($Re = 100$). While the total C_y acting on the entire wing is zero, each bristle is subject to a relatively large aerodynamic force that pushes the bristle away from the center of the wing.[12]

Next, we compare the forces acting on a bristled wing and a flat solid wing without gaps for $Re = 10$ (Fig. 9). For the solid wing, we obtain C_x and C_y acting on three separated segments, the locations of which correspond exactly to the locations of the first three bristles from the top (red, orange, and green) in Fig. 8. In Fig. 9(a), the trend that C_x has a greater peak magnitude and a delayed phase when the section is farther from the wing center is observed for both bristled and flat wings. Here, one of the noticeable features of the bristled wing, namely, a large force per actual wing area ($\frac{5}{9}c$ in our model), reported by Sunada $et\ al.$,[11] is also confirmed by the forces acting on the segments. The maximum positive C_x at a bristle

FIG. 8. x- and y-directional force coefficients for each of five bristles during one cycle: [(a) and (b)] $Re = 100$ and [(c) and (d)] $Re = 10$. Note the different ranges of C_x and C_y on the vertical axes. The colors of the curves correspond to the colors of the bristles shown on the right side of the figure (e.g., red for the uppermost bristle and black for the lowermost bristle).
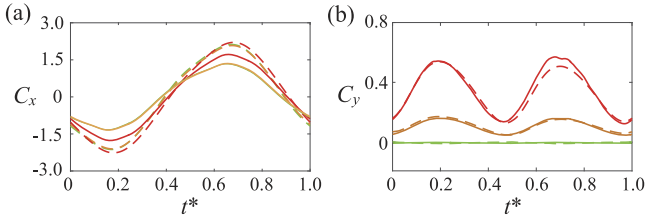
FIG. 9. Comparison of x- and y-directional force coefficients between a bristled wing (dashed curves) and a solid wing without gaps (solid curves) for $Re = 10$. The ranges of C_x and C_y are different. The colors of the curves correspond to the color of each bristle shown in Fig. 8. The solid wing has the same chord c as the bristled wing. The curves for the bristled wing are identical to the curves presented in Fig. 8.

is about 28% larger than that at the corresponding segment of the solid wing for the outer segment (red curve) and about 53% larger for the inner and center segments (orange and green curves).

The x-directional force C_x at the outer segment is affected by the strong outer-edge vortex, and this vortex is generated, regardless of the existence of a gap; see Fig. 3 (Multimedia view) for the outer-edge vortex of a bristled wing. Thus, the difference in C_x between the bristled and solid wings at the outer segment is not as pronounced as at the inner and center segments. However, C_y at each segment shows little difference between the bristled and solid wings [Fig. 9(b)]. That is, the viscous shear stress in the y-direction acting on a specific section is not strongly affected by the existence of a gap. The difference in C_x for the corresponding segments between the bristled and solid wings and the variation in C_y among the three segments indicate that the aerodynamic performance of the entire bristled wing should be evaluated in the context of the collective behavior of the bristles. The propulsive force generated by each bristle will be significantly affected by the relative positions of the bristles and their mutual interaction by viscous diffusion.

To examine the effect of gap flow on the C_y distribution in more detail, the y-directional force per unit area [$f_y = (\boldsymbol{n} \cdot \boldsymbol{\tau})_y$, $\boldsymbol{n}$: unit normal vector into the fluid domain and $\boldsymbol{\tau}$: viscous stress tensor] on the left and right surfaces of the wing is illustrated for the upper half of the wing in Fig. 10. At $Re = 100$, for

the solid wing, the y-directional force changes gradually on the two surfaces and has a positive value for most of the wing [Fig. 10(a)]. In general, the windward side of the wing (right surface at $t^* = 0.25$–0.50 and left surface at $t^* = 0.50$–0.75) has a larger C_f, and C_f on the windward side increases from the center to the upper edge. However, the flow through the gap changes the spatial distribution of C_f drastically. For the bristled wing at $Re = 100$, both the positive and negative C_f exist on the surface of each bristle [Fig. 10(b)]. The upper and lower edges of each bristle tend to have positive and negative C_f, respectively. The spatial gradient of C_f on the surface is found to be larger for the windward surface at $t^* = 0.25$ and 0.75, where the wing speed is largest. The tendency to produce both positive and negative C_f especially on the windward side is caused by a strong gap flow turning around the edges of each bristle, which can be inferred from the arrows showing the gap flow in Fig. 5(a).

On the other hand, for $Re = 10$, because of the virtual barrier effect of the gaps, the spatial distribution of C_f is not significantly different at the same location between the solid wing [Fig. 10(a)] and the bristled wing [Fig. 10(b)]. The similarity in the C_f distribution is obvious when compared with the $Re = 100$ case. This characteristic also explains the trend of similar C_y over a cycle between the corresponding segments of the two wings in Fig. 9(b). It is noteworthy that C_f is most similar at $t^* = 0.40$, when the gap flow relative to the wing is found to be minimal [Fig. 5(a)], and the biggest difference is observed at $t^* = 0.50$ (stroke reversal).

C. Flapping bristled wing

In Secs. III A and III B, we have used a wing model with a fixed angle of attack. Admittedly, for more realistic kinematics of the insect wing, we should take into consideration the periodic change in the angle of attack: flapping motion that combines oscillation and rotation [Fig. 1(d)]. Therefore, unlike the case of oscillation alone [Fig. 1(c)], asymmetry occurs in the flow structure, and the fluid force acting on a bristle is not symmetric with respect to the center of the wing. Basically, in flapping, the gap flow follows the same mechanism described in Subsections III A and III B, which depends strongly on the Reynolds number: for larger Reynolds
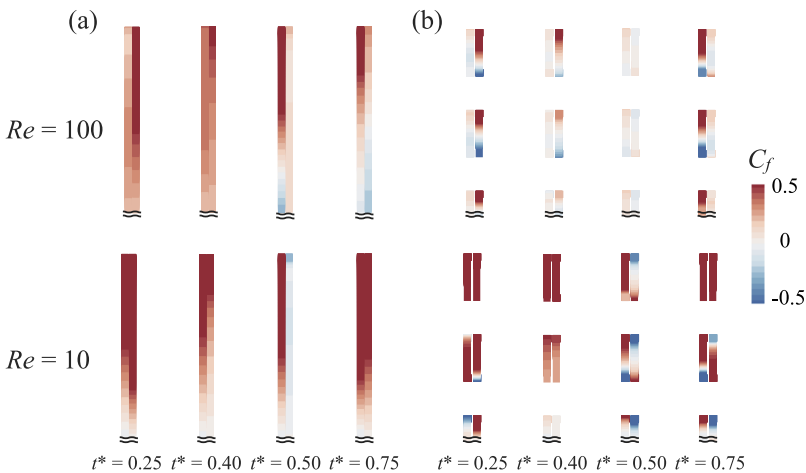

FIG. 10. Spatial distribution of the y-directional force per unit area ($C_f = 2f_y/\rho\overline{U}^2$) on the left and right surfaces of (a) a solid wing and (b) a bristled wing for $Re = 100$ and 10. The color in two adjacent columns of pixels indicates the magnitude of C_f on both the left surface (left column) and right surface (right column) of the wing. In this figure, only the upper half of the wing is presented and the thickness of the wing is magnified from its actual thickness.

numbers, the gap flow reacts more slowly to the kinematics of the wing. The phase and strength of gap vortices in the flapping bristled wing are analogous to the oscillating bristled wing for both $Re = 10$ and $Re = 100$ [Figs. 3(a) and 11 (Multimedia view)]. In the high-Reynolds-number regime, each bristle of a bristled wing seems to behave individually with regard to aerodynamic force generation, as we discussed in Sec. III B for the oscillating wing. In this subsection, therefore, we will focus on the effect of the asymmetry of the flow field and aerodynamic force due to the additional pitching motion for $Re = 10$.

During the deceleration phase, similar to the case of oscillation, a gap vortex is annihilated and almost disappears around $t^* = 0.40$, before reaching end-stroke [Fig. 11(b) (Multimedia view)]. Note that vorticity fields are almost identical between the solid wing and the bristled wing at $t^* = 0.40$ [Fig. 11(b) (Multimedia view)]. Then, at end-stroke, a gap vortex of opposite sign is clearly identified for all gaps. Also, the extinction of the leading-edge and trailing-edge vortices is slower than that of the gap vortex during the deceleration phase. Strong leading-edge and trailing-edge vortices can still be observed at $t^* = 0.40$, in contrast to the gap vortices, which is similar to what is seen in the case of an oscillating wing [Fig. 3 (Multimedia view)]. However, in contrast to the oscillating wing, for which the positive and negative vorticities in the gap are of almost equal magnitude, now the negative vorticity within the gap is dominant owing to convection of negative vorticity generated on the lower (pressure) surface of the wing.

(a) $Re = 100$

$t^* = 0.25$ $t^* = 0.40$ $t^* = 0.50$

(b) $Re = 10$

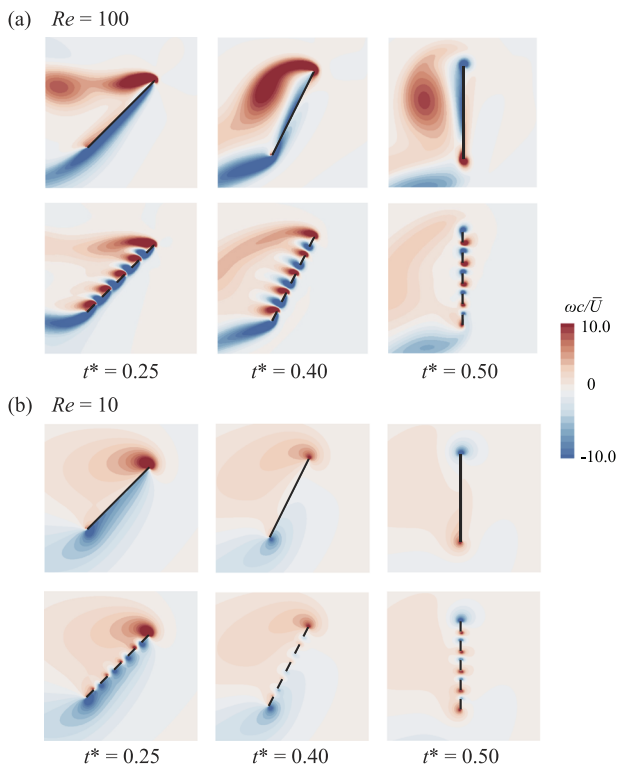$t^* = 0.25$ $t^* = 0.40$ $t^* = 0.50$

FIG. 11. Vortex structure around a solid wing (upper row) and a bristled wing (lower row) in flapping motion for (a) $Re = 100$ and (b) $Re = 10$. The black line represents the wing. In this figure, the thickness of the bristles i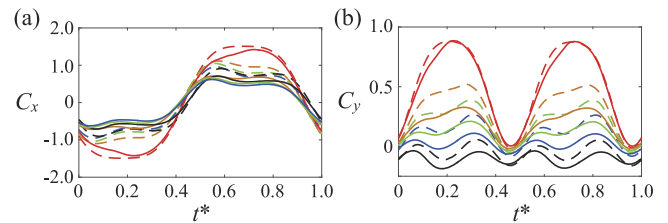s magnified from their actual thickness. Multimedia views: https://doi.org/10.1063/1.5030693.2 and https://doi.org/10.1063/1.5030693.3

FIG. 12. x- and y-directional force coefficients of five segments for a flapping wing during one cycle at $Re = 10$. The dashed curves are for a bristled wing and the solid curves for a solid wing. Note the different ranges of C_x and C_y. The color of each curve matches the colors in the model in Fig. 8.

With the approach similar to Fig. 9, Fig. 12 provides the forces acting on five bristles for the bristled wing and five segments at the corresponding positions for the solid wing. The forces acting on each segment show similar patterns for the solid and bristled wings, although their magnitudes are different. We have already explained that the difference in C_x between the solid and bristled wings is smaller at the outer segment than at the inner segment for an oscillating wing (Fig. 9). This trend is more pronounced in the case of flapping motion. For the segment closest to the leading edge (red, leading-edge segment), the maximum C_x of the solid wing is only about 5% smaller than that of the bristled wing and the maximum value of C_y is almost the same as that of the bristled wing. At a low Reynolds number, there is a large leading-edge vortex [red contour near the leading edge in Fig. 11(b) (Multimedia view)] that is not shed from the wing and is much greater than the gap vortex. For the flapping wing, the leading-edge vortex tilts closer to the wing compared with the corresponding outer vortex for the oscillating wing. Regarding force production of the leading-edge segment, the leading-edge vortex of the flapping wing makes a more significant contribution than the outer vortex of the oscillating wing, which means that the existence of the gap vortex becomes less critical in the flapping wing. Thus, the forces generated in the x- and y-directions at the leading-edge segment in the case of a bristled wing are similar to those generated in the case of a solid wing. For segments other than the leading-edge segment, C_x and C_y magnitudes of the bristled wing are generally greater than those of the solid wing, which is analogous to the trend observed in C_x for the oscillating wing [Fig. 9(a)].

IV. CONCLUDING REMARKS

For a bristled wing, we have numerically investigated the formation of gap flow during the unsteady motion of deceleration and stroke reversal and its effect on aerodynamic force acting on each bristle. Throughout this study, we have especially emphasized the Reynolds number dependence of the gap flow pattern. Even with a small change in the Reynolds number (from $Re = 10$ to $Re = 100$), for a bristled wing, a noticeable difference is observed in the formation of the gap vortex and the velocity distribution of the gap flow. We have shown that the reversal in the gap vorticity and the gap flow direction occurs more rapidly at a lower Reynolds number owing to stronger diffusion of vorticity and momentum, and the phase of the gap flow is strongly affected by the Reynolds number. While

each bristle behaves independently owing to strong gap flow at a higher Reynolds number, at a lower Reynolds number, a row of individual bristles behave collectively as if they were a continuous body as demonstrated in the noticeable variation in tangential force acting on the bristled wing among the bristles. For a flapping bristled wing, a unique trend of force generation for the bristle near the leading edge is found as a result of asymmetric leading-edge and trailing-edge vortex formation.

Although, in this study, fundamental aerodynamic principles have been explored for a periodic bristled wing, there has been no extensive consideration of different flapping kinematics. More importantly, our study is limited to a two-dimensional model. It should be noted that the bristled wings of the smallest insects are three-dimensional structures that undergo complex motions, which may complicate the formation of gap flow and its effect on the force generation of individual bristles. We conjecture that, if our bristled wing model has a finite span in a three-dimensional space, fluid can detour the wing in the spanwise direction, which may reduce the amount of gap flow and strengthen the effect of the virtual fluid barrier. For a three-dimensional bristled wing in translational motion, Lee and Kim[15] showed experimentally that a leading-edge vortex and a trailing-edge vortex can be formed even inside a virtually blocked gap between bristles positioned in the chordwise direction, which demonstrates that the study on three-dimensional effect is important to fully understand the aerodynamics of a bristled wing. Based on our findings in this study, in future work, we plan to study the aerodynamic performance of individual bristles and their mutual interaction in three-dimensional unsteady motions that are biologically more relevant.

ACKNOWLEDGMENTS

APPENDIX: VORTICITY THRESHOLDS FOR THE COMPUTATION OF CIRCULATION
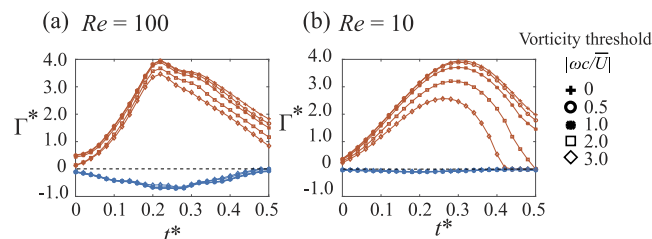

FIG. 13. Time history of nondimensional circulation $\Gamma^*(= \Gamma/\overline{U}c)$ for (a) $Re = 100$ and (b) $Re = 10$. The red color indicates positive circulation inside the solid area depicted at Fig. 4(c), and the blue color indicates negative circulation inside the dashed area of Fig. 4(c). Circulation is computed with several vorticity thresholds.

[1] T. Maxworthy, "The fluid-dynamics of insect flight," Annu. Rev. Fluid Mech. **13**, 329–350 (1981).
[2] C. P. Ellington, C. van den Berg, A. P. Willmott, and A. L. R. Thomas, "Leading-edge vortices in insect flight," Nature **384**, 626–630 (1996).
[3] M. H. Dickinson, F.-O. Lehmann, and S. P. Sane, "Wing rotation and the aerodynamic basis of insect flight," Science **284**, 1954–1960 (1999).
[4] P. J. George and J. T. Huber, "A new genus of fossil Mymaridae (Hymenoptera) from Cretaceous amber and key to Cretaceous mymarid genera," Zookeys **130**, 461–472 (2011).
[5] J. T. Huber and J. S. Noyes, "A new genus and species of fairyfly, *Tinkerbella nana* (Hymenoptera, Mymaridae), with comments on its sister genus *Kikiki*, and discussion on small size limits in arthropods," J. Hymenoptera Res. **32**, 17–44 (2013).
[6] K. E. Feith, A. F. Millett, S. P. Colin, J. O. Dabiri, and J. H. Costello, "Functional morphology and fluid interactions during early development of the scyphomedusa *Aurelia aurita*," Biol. Bull. **217**, 283–291 (2009).
[7] J. C. Nawroth, K. E. Feitl, S. P. Colin, J. H. Costello, and J. O. Dabiri, "Phenotypic plasticity in juvenile jellyfish medusae facilitates effective animal-fluid interaction," Biol. Lett. **6**, 389–393 (2010).
[8] A. Y. L. Cheer and M. A. R. Koehl, "Paddles and rakes: Fluid flow through bristles appendages of small organisms," J. Theor. Biol. **129**, 17–39 (1987).
[9] M. A. R. Koehl, "Small scale fluid dynamics of olfactory antennae," Mar. Freshwater Behav. Physiol. **27**, 127–141 (1996).
[10] M. A. R. Koehl, J. R. Koseff, J. P. Crimaldi, M. G. McCay, T. Cooper, M. B. Wiley, and P. A. Moore, "Lobster sniffing: Antennule design and hydrodynamic filtering of information in an odor plume," Science **294**, 1948–1951 (2001).
[11] S. Sunada, H. Takashima, T. Hattori, K. Yasuda, and K. Kawachi, "Fluid-dynamic characteristics of a bristled wing," J. Exp. Biol. **205**, 2737–2744 (2002), http://jeb.biologists.org/content/205/17/2737.
[12] E. Barta and D. Weihs, "Creeping flow around a finite row of slender bodies in close proximity," J. Fluid Mech. **551**, 1–17 (2006).
[13] D. Weihs and E. Barta, "Comb wings for flapping flight at extremely low Reynolds numbers," AIAA J. **46**, 285–288 (2008).
[14] G. Davidi and D. Weihs, "Flow around a comb wing in low-Reynolds-number flow," AIAA J. **50**, 249–253 (2012).
[15] S. H. Lee and D. Kim, "Aerodynamics of a translating comb-like plate inspired by a fairyfly wing," Phys. Fluids **29**, 081902 (2017).
[16] C. P. Ellington, "The aerodynamics of hovering insect flight. I. The quasi-steady analysis," Philos. Trans. R. Soc., B **305**, 1–15 (1984).
[17] A. Santhanakrishnan, A. K. Robinson, S. Jones, A. Lowe, S. Gadi, T. L. Hedrick, and L. A. Miller, "Clap and fling mechanism with interacting porous wings in tiny insect flight," J. Exp. Biol. **217**, 3898–3909 (2014).
[18] S. K. Jones, Y. J. J. Yun, T. L. Hedrick, B. E. Griffith, and L. A. Miller, "Bristles reduce the force required to 'fling' wings apart in the smallest insects," J. Exp. Biol. **219**, 3759–3772 (2016).
[19] C. H. K. Williamson, "Three-dimensional wake transition," J. Fluid Mech. **328**, 345–407 (1996).
[20] A. Gilmanov and F. Sotiropoulos, "A hybrid Cartesian/immersed boundary method for simulating flows with 3D geometrically complex moving bodies," J. Comput. Phys. **207**, 457–492 (2005).
[21] L. Ge and F. Sotiropoulos, "A numerical method for solving the 3D unsteady incompressible Navier-Stokes equations in curvilinear domains with complex immersed boundaries," J. Comput. Phys. **225**, 1782–1809 (2007).
[22] I. Borazjani, L. Ge, and F. Sotiropoulos, "Curvilinear immersed boundary method for simulating fluid structure interaction with complex 3D rigid bodies," J. Comput. Phys. **227**, 7587–7620 (2008).
[23] Y. Saad and M. H. Schultz, "GMRES: A generalized minimal residual algorithm for solving nonsymmetric linear systems," SIAM J. Sci. Stat. Comput. **7**, 856–869 (1986).
[24] P. N. Brown and Y. Saad, "Hybrid Krylov methods for nonlinear systems of equations," SIAM J. Sci. Stat. Comput. **11**, 450–481 (1990).
[25] J. Van Kan, "A second-order accurate pressure-correction scheme for viscous incompressible flow," SIAM J. Sci. Stat. Comput. **7**, 870–891 (1986).
[26] H. Dütsch, F. Durst, S. Becker, and H. Lienhart, "Low-Reynolds-number flow around an oscillating circular cylinder at low Keulegan-Carpenter numbers," J. Fluid Mech. **360**, 249–271 (1998).

[27]D. J. Tritton, "Experiments on the flow past a circular cylinder at low Reynolds numbers," J. Fluid Mech. **6**, 547–567 (1959).

[28]A. E. Hamielec and J. D. Raal, "Numerical studies of viscous flow around circular cylinders," Phys. Fluids **12**, 11 (1969).

[29]G. J. Sheard, K. Hourigan, and M. C. Thompson, "Computations of the drag coefficients for low-Reynolds number flow past rings," J. Fluid Mech. **526**, 257–275 (2005).

[30]N. Vandenberghe, J. Zhang, and S. Childress, "Symmetry breaking leads to forward flapping flight," J. Fluid Mech. **506**, 147–155 (2004).

[31]D. Kim and M. Gharib, "Characteristics of vortex formation and thrust performance in drag-based paddling propulsion," J. Exp. Biol. **214**, 2283–2291 (2011).

[32]E. Barta, "Motion of slender bodies in unsteady Stokes flow," J. Fluid Mech. **688**, 66–87 (2011).